Strain-controlled evolution of electronic structure indicating topological phase transition in the quasi-one-dimensional superconductor math xmlns="http://www.w3.org/1998/Math/MathML">msub>mi>TaSe/mi>mn>3/mn>/msub>/math>

Jounghoon Hyun, Min Yong Jeong, Myung-Chul Jung, Yeonghoon Lee, Younsik Kim, Saegyeol Jung, Byeongjun Seok, Junseong Song, Chan-young Lim, Jaehun Cha, Gyubin Lee, Yeojin An, Makoto Hashimoto, Donghui Lu, Jonathan D. Denlinger, Sung Wng Kim, Changyoung Kim, Myung Joon Han, Sunghun Kim, and Yeongkwan Kim

Strain-controlled evolution of electronic structure indicating topological phase transition in a quasi-one-dimensional superconductor TaSe$_3$

Jounghoon Hyun,[1] Min Yong Jeong,[1] Myung-Chul Jung,[1] Yeonghoon Lee,[1] Younsik Kim,[2,3] Saegyeol Jung,[2,3] Byeongjun Seok,[2,3] Junseong Song,[4] Chan-young Lim,[1] Jaehun Cha,[1] Gyubin Lee,[1] Yeojin An,[1] Makoto Hashimoto,[5] Donghui Lu,[5] Jonathan D. Denlinger,[6] Sung Wng Kim,[4,7] Changyoung Kim,[2,3] Myung Joon Han,[1,*] Sunghun Kim,[1,†] and Yeongkwan Kim[1,‡]

[1]*Department of Physics, Korea Advanced Institute of Science and Technology, Daejeon 34141, Republic of Korea.*
[2]*Center for Correlated Electron Systems, Institute for Basic Science, Seoul 08826, Republic of Korea.*
[3]*Department of Physics and Astronomy, Seoul National University, Seoul 08826, Republic of Korea.*
[4]*Department of Energy Science, Sungkyunkwan University, Suwon 16419, Republic of Korea.*
[5]*Stanford Synchrotron Radiation Lightsource, Stanford Linear Accelerator Center, Menlo Park, CA 94025, USA.*
[6]*Advanced Light Source, Lawrence Berkeley National Laboratory, Berkeley, CA 94720, USA.*
[7]*Center for Integrated Nanostructure Physics, Institute for Basic Science, Suwon 16419, Republic of Korea.*
(Dated: March 22, 2022)

We report a signature of strain-controlled topological phase transition in the electronic structure of a quasi-one-dimensional superconductor TaSe$_3$. Using angle-resolved photoemission spectroscopy and first-principles calculation, TaSe$_3$ is identified to be in a weak topological insulator phase which has topologically nontrivial surface states only at the allowed planes. Under uniaxial tensile strain, Dirac point and the topological surface state emerge on the originally forbidden $(10\bar{1})$ plane, which demonstrates the transition to a strong topological insulator phase. Our results accomplish the experimental realization of possible topological insulating phases in TaSe$_3$ and highlight a unique possibility of coupling the superconductivity with two distinct topological insulating phases in a controllable manner.

The discovery of topological insulators (TIs) has triggered an intensive search for diverse topological materials. For instance, strong/weak Z_2 TIs [1–5], topological crystalline insulators [6, 7], Dirac/Weyl semimetals [8, 9], and topological superconductors (TSCs) have been explored and successfully identified [10–14]. In particular, TSCs have attracted great interest since their Majorana quasiparticles can be utilized for quantum computation [15]. In searching for TSCs, intensively investigated are the heterostructure systems based on superconducting proximity effect [10, 11] and the superconductors which possess topological surface state (TSS) [13, 14]. So far, most of the previous studies have been carried out on the systems coupled with strong TI (STI).

A quasi-one-dimensional (quasi-1D) superconductor TaSe$_3$ ($T_C \sim 2$ K) [16, 17] can be a promising material which allows us to explore novel superconductivity in connection with its topological property. In addition to its unusual behavior of the absence of diamagnetic response below T_C [18], the nontrivial topological phase of this material has recently been suggested by the first-principles calculation [19] and supported by transport measurements [20–22] as well as photoemission spectroscopy studies [23, 24]. More intriguingly, the calculation predicts that this material locates near the boundary between STI and weak topological insulator (WTI) phases depending on its lattice sizes [19]. Indeed, recent photoemission studies observed STI phase [23, 24] whereas the transport measurement reports the absence of TSS signal [22], indicative of the possible WTI phase rather than STI. Putting all these things together, the

previous investigations seem to indicate that TaSe$_3$ is a unique superconducting system whose topological phase can easily be changed by external or internal stimuli such as strain. This exciting possibility of controllable topological phase transition coexisting with superconductivity is the main motivation of current study.

In this Letter, we report a detailed study on the electronic structure and topological phases of TaSe$_3$ by angle-resolved photoemission spectroscopy (ARPES) and first-principles density functional theory (DFT) calculation. The topologically nontrivial band structure was observed with the gap induced by band inversion, while the TSS is absent on $(10\bar{1})$ cleavage plane. Together with the analysis of Z_2 topological invariants, the topological nature of TaSe$_3$ is identified to belong to a WTI phase. Furthermore, we successfully induced topological phase transition into the STI phase by applying tensile strain, which is signaled by the appearance of the TSS on the same $(10\bar{1})$ plane. Our work suggests TaSe$_3$ as a unique platform to explore the interplay between superconductivity and two distinct topological phases in a controlled manner.

Single crystals of TaSe$_3$ with a typical size of $10 \times 1 \times 0.05$ mm^3 were grown by chemical vapor transport (Fig. 1(a)). Electrical transport measurement indicates the high quality of crystal with a residual resistance ratio (RRR, R(300 K)/R(1.9 K)) ~ 80 and the superconductivity with the drop of resistance below ~ 2 K (Fig. 1(b)). Synchrotron-based ARPES measurements were performed at beamlines 5-4, 5-2 of Stanford Synchrotron Radiation Lightsource (SSRL) and beamline
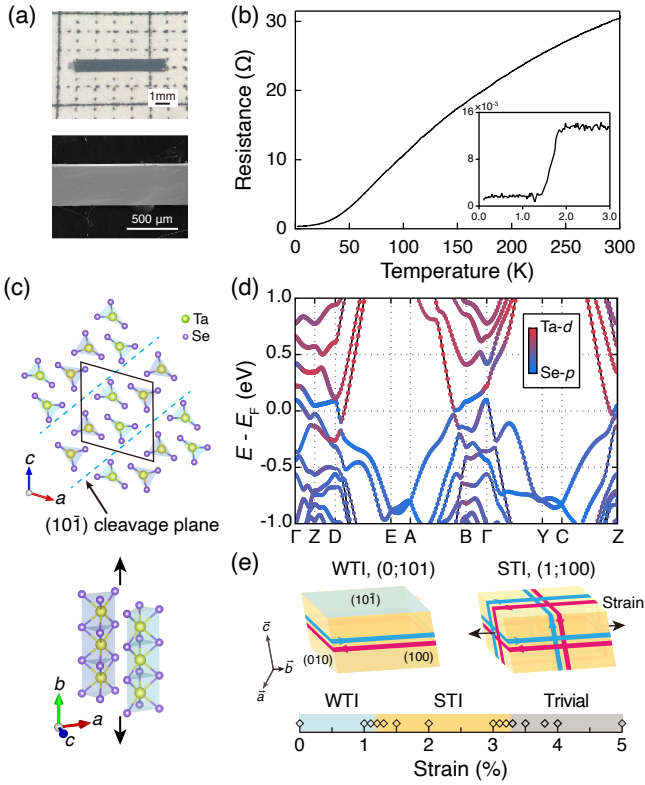
FIG. 1. (a) Images of TaSe$_3$ single crystal. (b) Temperature-dependent resistance along the chain direction. Inset shows the superconducting transition at ~ 2 K. (c) Crystal structure of TaSe$_3$. Black solid parallelogram and blue dashed lines indicate the unit cell and the practical cleavage plane $(10\bar{1})$, respectively. (d) Calculated bulk band structure of TaSe$_3$ with spin-orbit coupling. The weight of Ta-5d and Se-4p orbitals are presented by red and blue colors, respectively. (e) Schematic illustrations of WTI (left) and STI (right) phases in TaSe$_3$. Below is calculated topological phase diagram as a function of tensile strain along the b-axis. Markers indicate points that calculations are conducted.

FIG. 2. (a) 3D and surface-projected BZs of TaSe$_3$. The blue plane represents $(10\bar{1})$ surface BZ. (b) FS measured on the $(10\bar{1})$ plane ($h\nu = 20$ eV). (c),(d) Band dispersion along (c) $\tilde{\Gamma}$–$\tilde{Y}$ and (d) $\tilde{X}$–$\tilde{S}$ measured by ARPES using LV (left) and LH (right) polarized light. (e),(f) Entire band dispersions obtained by adding up the spectra from different polarized lights in (c),(d). Overlaid black dashed lines are the calculated bulk bands along (e) Γ–Y and (f) Z–C. Red arrows indicate additional hole bands which are not reproduced in the bulk band calculation.

4.0.3 of Advanced Light Source (ALS). High-resolution laser-based ARPES measurements were conducted at Center for Correlated Electron Systems, Institute for Basic Science. Samples were cleaved at 10 K under ultra-high vacuum with the pressure better than 5×10^{-11} Torr. Total energy resolution was set to be better than 10 meV for synchrotron-based and 4 meV for laser-based experiments [25]. Photon energies used for each measurements are given in the caption. DFT band calculations were carried out with Vienna Ab initio Simulation Package (VASP) based on the projector augmented-wave pseudopotential [26, 27] in consideration of spin-orbit coupling (SOC). Main results were obtained within 'PBE' generalized gradient approximation (GGA) for exchange-correlation functional [28]. Other functionals, including GGA-PBEsol [29], local density approximation (LDA) [30, 31], and modified Becke-Johnson (mBJ) [32–34], were also used for comparison. The maximally local-

ized Wannier functions (MLWFs), as generated by "Wannier90" code [35–37], were used for the analysis of topological invariants. For the surface electronic structure calculations, we adopted "WannierTools" [38, 39]. The topological nature of TaSe$_3$ is double-checked by using "Wien2k" [40] and "Vasp2trace" [41] software package.

TaSe$_3$ has a quasi-1D monoclinic P2$_1$/m crystal structure [42] with prismatic chains elongating along the b-axis. The chains are stacked via van der Waals interaction with a natural cleavage plane of $(10\bar{1})$ surface (Fig. 1(c)). The calculated bulk band structure along the high-symmetry lines of three-dimensional (3D) Brillouin zone (BZ) shows that the low-energy electronic states are governed by Ta-5d and Se-4p orbital characters, whose weights are depicted by red and blue colors, respectively (Fig. 1(d)). The orbital-weighted band structure shows the band inversions along D-E, B-A, and Z-C high-symmetry lines, which indicates a nontrivial topology of the electronic structure. The band inversion and gap opening become clearer in comparison to the calculated band structure without SOC [25]. Based on the band inversions, the band parity at time-reversal invariant momenta (TRIM) were calculated to understand the topological nature of TaSe$_3$. The result shows that the parity of the highest occupied band changes at Z and B,
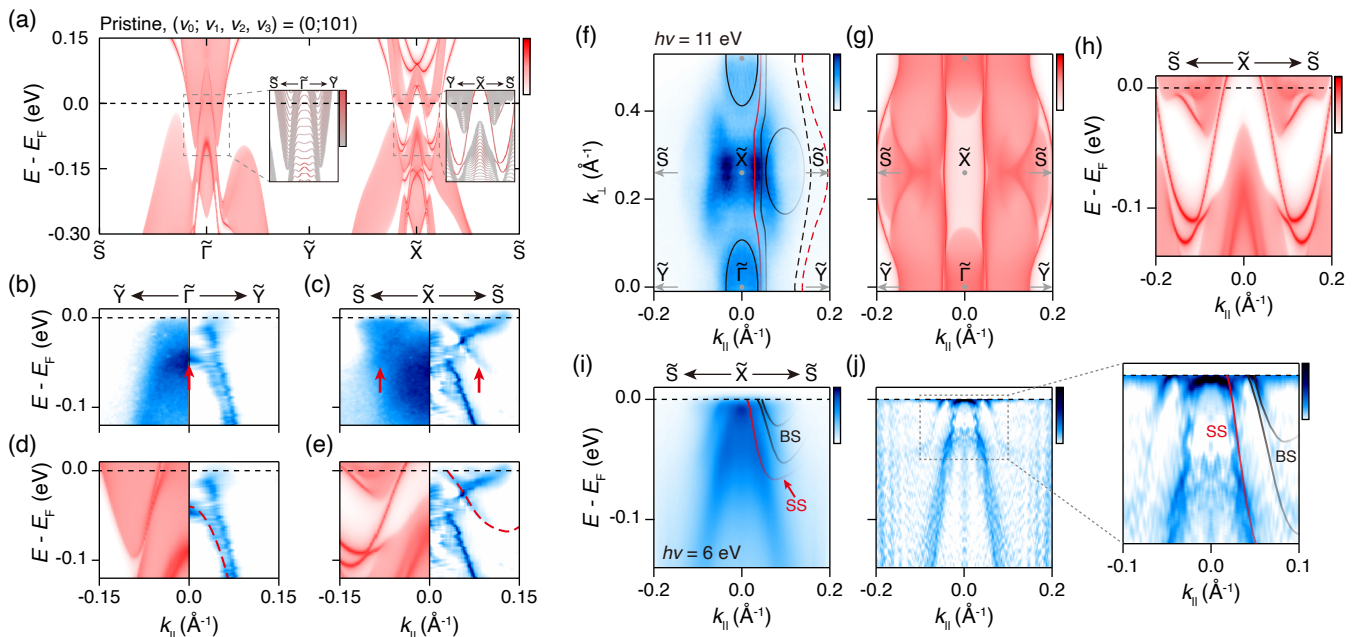
FIG. 3. (a) Calculated surface electronic structure on the $(10\bar{1})$ surface of pristine TaSe$_3$. The results in the areas closed by the gray dashed box are magnified in the insets. (b),(c) Zoomed-in ARPES spectra (left) and the curvature plots (right) along (b) $\tilde{\Gamma}$–$\tilde{Y}$ and (c) $\tilde{X}$–$\tilde{S}$ of Fig. 2(e),(f). (d),(e) Curvature plots compared with the calculated band structure taken from (a). Red dashed lines are the guides to the eye for the additional hole bands indicated by red arrows in (b),(c). (f),(g) FS obtained by (f) laser-based ARPES ($h\nu = 11$ eV) and (g) the calculation. Overlaid solid and dashed lines are guides to the eye for the FS, of which colors represent BS (black) and SS (red). Dashed lines indicate invisible parts of FS in this photon energy [25]. (h) Band dispersion along $\tilde{X}$–$\tilde{S}$ taken from (a). (i) Band dispersion along $\tilde{X}$–$\tilde{S}$, measured by laser-based ARPES ($h\nu = 6$ eV) (j) Curvature plot of (i) and its zoomed-in image. Overlaid lines are guides to the eye for the band dispersion.

which renders a WTI phase of the pristine TaSe$_3$ with topological invariants $(\nu_0;\nu_1,\nu_2,\nu_3) = (0;101)$.

The quasi-1D structure makes the system to be easily affected by the uniaxial strain along the chain direction, which can also modify the topological phase. To check the effect of the strain, DFT calculations were carried out. Interestingly, by increasing the tensile strain along the b-axis (black arrows in Fig. 1(c)), the band inversions at Z and B sequentially disappear [25]. It drives the topological phase transition from WTI to STI characterized by topological invariants (1;100) above ~ 1.2 % of strain and another transition to a trivial insulator phase with more than ~ 3.3 % of strain Fig. 1(e) [25]. Note that a similar trend was previously reported in a theoretical study [19] although identification of the topological nature of pristine TaSe$_3$ has a critical dependence on the exchange-correlation functional choice [25]. An important difference between WTI and STI is that WTI has topologically dark surfaces, where TSS is absent, while STI hosts TSS on every surface. In case of WTI, the topologically dark surface is determined by the topological invariants (ν_1,ν_2,ν_3) [1], which is $(10\bar{1})$ surface for the pristine TaSe$_3$. Thus, the $(10\bar{1})$ plane is the key surface in characterizing the topological nature and the phase transition of this material.

To examine the electronic structure of TaSe$_3$, ARPES

measurement was performed on the $(10\bar{1})$ surface. The observed Fermi surface (FS) elongating perpendicular to the chain direction $(k_\perp)$ reflects the quasi-1D character (Fig. 2(b)). In particular, we focus on the band dispersion along $\tilde{\Gamma}$–$\tilde{Y}$ and $\tilde{X}$–$\tilde{S}$ high-symmetry lines as the bulk high-symmetry lines involving band inversions are projected onto these lines (Fig. 2(a)). Both linear vertically (LV) and linear horizontally (LH) polarized light were utilized to prevent any loss of the spectral weight due to the matrix element effect. Indeed, each result taken with different polarizations visualizes different bands (Fig. 2(c),(d)) so that both results are added up to capture the entire band dispersion (Fig. 2(e),(f)). Overall band structure along $\tilde{\Gamma}$–$\tilde{Y}$ and $\tilde{X}$–$\tilde{S}$ are in agreement with the bulk band calculation along Γ–Y and Z–C (black dashed lines in Fig. 2(e),(f)), respectively, including the gap induced by band inversion around $\tilde{X}$ near the E_F characterized by two separated electron bands and one hole band located below [43]. However, there are some bands that are not reproduced by the bulk band calculation, for example, the additional hole band at $\tilde{\Gamma}$ and the tiny hole band around $\tilde{X}$ located inside the gap indicated by red arrows in Fig. 2(e),(f), which are also found in zoomed-in images below (Fig. 3(b),(c)).

In order to elucidate the origin of these additional bands, we conducted surface electronic structure calcula-
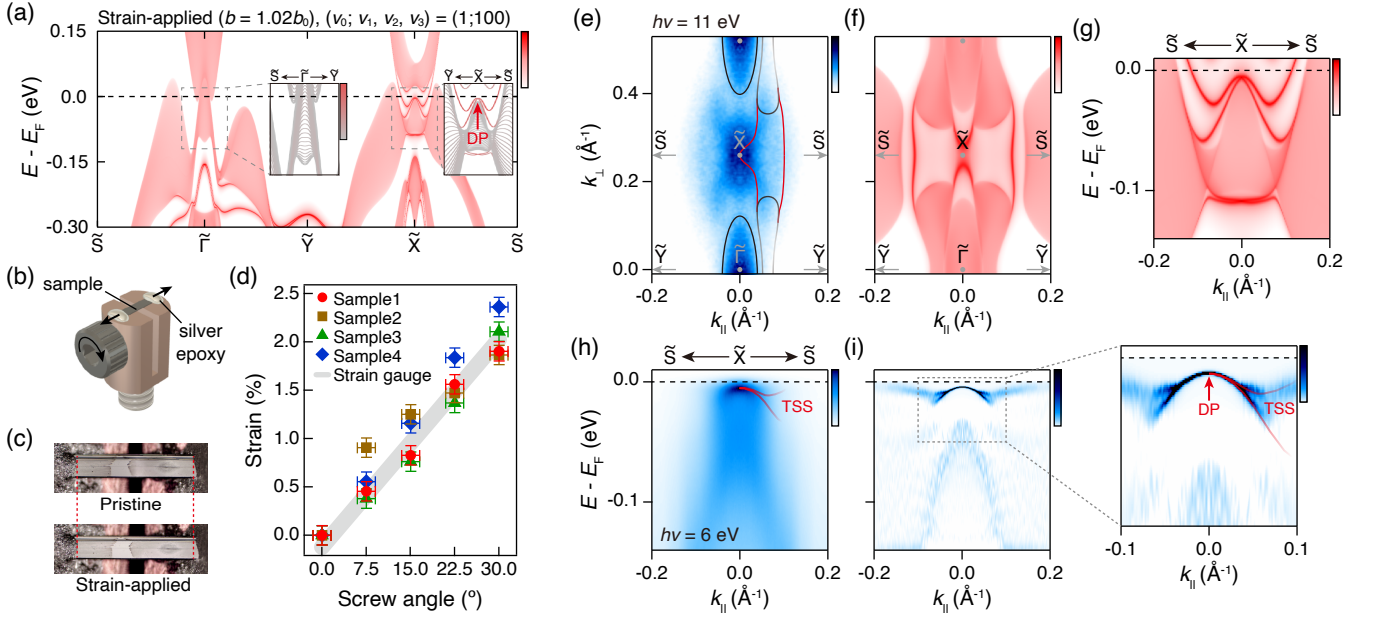
FIG. 4. (a) Calculated surface electronic structure on the ($10\bar{1}$) surface, under 2 % of tensile strain along the b-axis. A red arrow in the inset indicates the Dirac point at $\tilde{X}$. (b) Illustration of a sample holder designed to apply strain. (c) Microscopic images of pristine (upper) and strain-applied (lower) sample. Red dashed lines indicate both end positions of the pristine sample. (d) Screw angle-dependent strain plots obtained by analyzing the length of the samples. Gray line is a fitted line of strain plots obtained by strain gauges [25]. (e),(f) FS of strain-applied TaSe$_3$ obtained by (e) laser-based ARPES ($h\nu = 11$ eV) and (f) the calculation. Overlaid solid lines are guides to the eye for the FS, of which colors represent BS (black) and SS (red). (g) Band dispersion along $\tilde{X}$–$\tilde{S}$ taken from (a). (h) Band dispersion along $\tilde{X}$–$\tilde{S}$, measured by laser-based ARPES ($h\nu = 6$ eV) (i) Curvature plot of (h) and its zoomed-in image. Overlaid lines are guides to the eye for the topological surface state.

tion on the ($10\bar{1}$) plane (Fig. 3(a)) showing surface states near $\tilde{\Gamma}$ and $\tilde{X}$ that are well separated from the projected bulk continuum. In Fig. 3(d),(e), the calculated results are compared with curvature plots [44] of ARPES spectra (right panels of Fig. 3(b),(c)). The calculated surface electronic structure reproduces the observed ARPES spectra and unveils the surface origin of the extra bands, which is further confirmed by comparing ARPES spectra measured at several photon energies, examining the k_z independent dispersion of the bands [25].

The band topology was further investigated with higher-resolution laser-based ARPES measurement. Figure 3(f) shows the observed ($10\bar{1}$) FS which agrees well with the one in Fig. 2(b). The entire band structure is analyzed along $k_\parallel$ at several different $k_\perp$ points between $\tilde{\Gamma}$ and $\tilde{X}$ by tracing the dispersion of each band [25]. The analysis reveals a hole pocket centered at $\tilde{\Gamma}$, two electron-like Fermi sheets through the whole BZ, and an electron pocket near $\tilde{X}$. The origins of FSs are classified by accounting the calculated band (Fig. 3(g)) into bulk state (BS) (black) and surface state (SS) (red); see the overlaid guidelines in Fig. 3(f). Focusing on the bands crossing E_F along $\tilde{X}$–$\tilde{S}$ (Fig. 3(h)-(j)), three bands are identified; one SS and two BSs. The SS locates inside the bulk band gap and crosses E_F twice (Fig. 3(a)), not merging into the valence band. Also, there is no other SS to form the

Dirac point (DP) at $\tilde{X}$. Therefore, SS around $\tilde{X}$ cannot be attributed to TSS. The absence of TSS evidences that ($10\bar{1}$) plane is topologically dark, confirming the WTI nature of pristine TaSe$_3$.

Next, we examine the strain-induced changes of the band structure and its topology. As noted in the phase diagram of Fig. 1(e), the tensile strain of 1.2 – 3.3 % can drive a topological phase transition to STI. In fact, the calculated surface band structure with 2 % of tensile strain along the b-axis clearly shows the Dirac point at $\tilde{X}$ (Fig. 4(a)) which is consistent with the STI phase expected from the calculated topological invariants (1;100). It is distinct from the result of the pristine case in which DP is absent at $\tilde{X}$ (Fig. 3(a)). To confirm it, we applied the uniaxial tensile strain using a sample holder as shown in Fig. 4(b) [45]. The actual value of the strain controlled by rotating a screw, is estimated both by the strain gauge and by analyzing the length of the sample from the optical microscopic images (Fig. 4(c)) [25], as summarized in Fig. 4(d). Based on these results, we verified that the appropriate strain (~ 2 %) is applied to the sample.

Figure 4(e) shows the FS measured on the ($10\bar{1}$) plane for the strain-applied sample. The same analysis with the above was carried out to classify each FS [25] and the same color codes were used to indicate BS and SS. Dif-

ferent from the pristine sample, a hole pocket centered at $\tilde{\Gamma}$ and a narrow electron pocket along $\tilde{\Gamma}$–$\tilde{Y}$ are observed, which are originated from the bulk. On the other hand, two surface-originated bands cross at $\tilde{X}$ slightly below E_F (Fig. 4(g)-(i)). Notably, only one SS band disperses above E_F after crossing at $\tilde{X}$ and eventually merges into the conduction band, while the other SS band goes into the below valence band. The observed SS band, that connects the valence and conduction band and crosses at TRIM, strongly indicates the characteristics of the TSS. This result therefore provides convincing evidence that $(10\bar{1})$ plane is no longer topologically dark and the system became to have a STI phase under the given strain.

We note that recent ARPES studies identify TSS on the $(10\bar{1})$ surface of pristine TaSe$_3$ [23, 24], and a transition into a trivial insulator was induced by tensile strain [24], which is different from our observation. The discrepancy would be attributed to the internal strain in the sample. Given that TaSe$_3$ locates in the vicinity of the WTI–STI phase boundary (Fig. 1(e)), Se vacancies in the as-grown single crystal can generate the unexpected internal strain which is sufficient to alter the topological phase of TaSe$_3$. Indeed, in the presence of Se vacancy, e.g. TaSe$_{2.9}$, the DFT total energy has minimum at the larger lattice constant, which corresponds to ~ 2 % of tensile strain [25]. This demonstrates that the internal strain can be built by Se vacancy, and it could be strong enough to switch the topological phase of the pristine state. Furthermore, even in the same topological phase, our calculation reveals that detailed band dispersion alters depending on relatively small lattice size difference within 1 % which further supports that the present system is highly sensitive to the little variation of the lattice constant [25].

By confirming the existence of the WTI phase, our work completes the strain phase diagram of superconducting TaSe$_3$ and demonstrates the transition into different topologically nontrivial phase, STI. This material can thus serve as an unprecedented platform to study the intriguing interplay between superconductivity and two different TI phases. For instance, in WTI, TSS has quasi-1D band dispersion which mimics the 1D topological edge state of two-dimensional TIs. Due to the spin-momentum locking, the spin directions are mostly antiparallel in the whole BZ so that the backscattering is fully prohibited, resulting more robust TSS [4, 46]. In case of STI, the partial skew scattering is allowed due to the closed FS [47]. Thus, it would be expected that the superconductivity coupled with WTI phase gives rise to the more stable state. Furthermore, the controllability of topological phases provides an exciting opportunity to manipulate TSS and Majorana quasiparticles on certain surfaces. We believe that further investigation on this topologically nontrivial superconductor will expand our knowledge of the exotic superconductivity.

———

[*] mj.han@kaist.ac.kr
[†] sunghun.kim@kaist.ac.kr
[‡] yeongkwan@kaist.ac.kr

[1] L. Fu, C. L. Kane, and E. J. Mele, Phys. Rev. Lett. **98**, 106803 (2007).

[2] D. Hsieh, D. Qian, L. Wray, Y. Xia, Y. S. Hor, R. J. Cava, and M. Z. Hasan, Nature **452**, 970 (2008).

[3] Y. L. Chen, J. G. Analytis, J.-H. Chu, Z. K. Liu, S.-K. Mo, X. L. Qi, H. J. Zhang, D. H. Lu, X. Dai, Z. Fang, S. C. Zhang, I. R. Fisher, Z. Hussain, and Z.-X. Shen, Science **325**, 178 (2009).

[4] C. Pauly, B. Rasche, K. Koepernik, M. Liebmann, M. Pratzer, M. Richter, J. Kellner, M. Eschbach, B. Kaufmann, L. Plucinski, C. M. Schneider, M. Ruck, J. van den Brink, and M. Morgenstern, Nat. Phys. **11**, 338 (2015)

[5] R. Noguchi, T. Takahashi, K. Kuroda, M. Ochi, T. Shirasawa, M. Sakano, C. Bareille, M. Nakayama, M. D. Watson, K. Yaji, A. Harasawa, H. Iwasawa, P. Dudin, T. K. Kim, M. Hoesch, V. Kandyba, A. Giampietri, A. Barinov, S. Shin, R. Arita, T. Sasagawa, and T. Kondo, Nature **566**, 518 (2019).

[6] Y. Tanaka, Z. Ren, T. Sato, K. Nakayama, S. Souma, T. Takahashi, K. Segawa, and Y. Ando, Nat. Phys. **8**, 800 (2012).

[7] Y. Ando and L. Fu, Annu. Rev. Condens. Matter Phys. **6**, 361 (2015).

[8] Z. K. Liu, B. Zhou, Y. Zhang, Z. J. Wang, H. M. Weng, D. Prabhakaran, S.-K. Mo, Z. X. Shen, Z. Fang, X. Dai, Z. Hussain, and Y. L. Chen, Science **343**, 864 (2014).

[9] S.-Y. Xu, I. Belopolski, N. Alidoust, M. Neupane, G. Bian, C. Zhang, R. Sankar, G. Chang, Z. Yuan, C.-C. Lee, S.-M. Huang, H. Zheng, J. Ma, D. S. Sanchez, B. Wang, A. Bansil, F. Chou, P. P. Shibayev, H. Lin, S. Jia, and M. Z. Hasan, Science **349**, 613 (2015).

[10] L. Fu and C. L. Kane, Phys. Rev. Lett. **100**, 096407(2008).

[11] J.-P. Xu, M.-X. Wang, Z. L. Liu, J.-F. Ge, X. Yang, C. Liu, Z. A. Xu, D. Guan, C. L. Gao, D. Qian, Y. Liu, Q.-H. Wang, F.-C. Zhang, Q.-K. Xue, and J.-F. Jia, Phys.

Rev. Lett. **114**, 017001 (2015).

[12] M. Sato and Y. Ando, Rep. Prog. Phys. **80**, 076501 (2017).

[13] Z. Wang, P. Zhang, G. Xu, L. K. Zeng, H. Miao, X. Xu, T. Qian, H. Weng, P. Richard, A. V. Fedorov, H. Ding, X. Dai, and Z. Fang, Phys. Rev. B **92**, 115119 (2015).

[14] P. Zhang, K. Yaji, T. Hashimoto, Y. Ota, T. Kondo, K. Okazaki, Z. Wang, J. Wen, G. D. Gu, H. Ding, and S. Shin, Science **360**, 182 (2018).

[15] J. Alicea, Rep. Prog. Phys. **75**, 076501 (2012).

[16] T. Sambongi, M. Yamamoto, K. Tsutsumi, Y. Shiozaki, K. Yamaya, and Y. Abe, J. Phys. Soc. Jpn. **42**, 1421 (1977).

[17] M. Yamamoto, J. Phys. Soc. Jpn. **45**, 431 (1978).

[18] S. Nagata, S. Ebisu,T. Aochi,Y. Kinoshita, S. Chikazawa, and K. Yamaya, J. Phys. Chem. Solids **52**, 761 (1991).

[19] S. Nie, L. Xing, R. Jin, W. Xie, Z. Wang, and F. B. Prinz, Phys. Rev. B **98**, 125143 (2018).

[20] W. Xia, X. Shi, Y. Zhang, H. Su, Q. Wang, L. Ding, L. Chen, X. Wang, Z. Zou, N. Yu, L. Pi, Y. Hao, B. Li, Z. Zhu, W. Zhao, X. Kou, and Y. Guo, Phys. Rev. B **101**, 155117 (2020).

[21] A. I. U. Saleheen, R. Chapai, L. Xing, R. Nepal, D. Gong, X. Gui, W. Xie, D. P. Young, E. W. Plummer, and R. Jin, npj Quantum Mater. **5**, 53 (2020).

[22] Y. Zhang, T. Zhu, H. Bu, Z. Cai, C. Xi, B. Chen, B. Wei, D. Lin, H. Xie, M. Naveed, X. Xi, F. Fei, H. Zhang, and F. Song, AIP Adv. **10**, 095314 (2020).

[23] C. Chen, A. Liang, S. Liu, S. Nie, J. Huang, M. Wang, Y. Li, D. Pei, H. Yang, H. Zheng, Y. Zhang, D. Lu, M. Hashimoto, A. Barinov, C. Jozwiak, A. Bostwick, E. Rotenberg, X. Kou, L. Yang, Y. Guo, Z. Wang, H. Yuan, Z. Liu, and Y. Chen, Matter **3**, 2055 (2020).

[24] C. Lin, M. Ochi, R. Noguchi, K. Kuroda, M. Sakoda, A. Nomura, M. Tsubota, P. Zhang, C. Bareille, K. Kurokawa, Y. Arai, K. Kawaguchi, H. Tanaka, K. Yaji, A. Harasawa, M. Hashimoto, D. Lu, S. Shin, R. Arita, S. Tanda, and T. Kondo, Nat. Mater. **20**, 1093 (2021)

[25] See Supplemental Material at URL for sample synthesis, computational details and complementary data.

[26] G. Kresse and J. Hafner, Phys. Rev. B **48**, 13115 (1993).

[27] G. Kresse and J. Furthmüller, Comput. Mater. Sci. **6**, 15(1996).

[28] J. P. Perdew, K. Burke, and M. Ernzerhof, Phys. Rev.Lett.**77**, 3865 (1996).

[29] G. I. Csonka, J. P. Perdew, A. Ruzsinszky, P. H. T.Philipsen, S. Lebègue, J. Paier, O. A. Vydrov, and J. G. Ángyán, Phys. Rev. B **79**, 155107 (2009).

[30] D. M. Ceperley and B. J. Alder, Phys. Rev. Lett. **45**, 566 (1980).

[31] J. P. Perdew and A. Zunger, Phys. Rev. B **23**, 5048 (1981).

[32] F. Tran and P. Blaha, Phys. Rev. Lett. **102**, 226401 (2009).

[33] D. J. Singh, Phys. Rev. B **82**, 205102 (2010)

[34] D. Koller, F. Tran, and P. Blaha, Phys. Rev. B **83**, 195134 (2011)

[35] N. Marzari and D. Vanderbilt, Phys. Rev. B **56**, 12847 (1997).

[36] I. Souza, N. Marzari, and D. Vanderbilt, Phys. Rev. B **65**, 035109 (2001).

[37] A. A. Mostofi, J. R. Yates, Y.-S. Lee, I. Souza, D. Vanderbilt, and N. Marzari, Comput. Phys. Commun. **178**, 685 (2008).

[38] M. P. L. Sancho, J. M. L. Sancho, and J. Rubio, J. Phys. F: Met. Phys. **15**, 851 (1985).

[39] Q. Wu, S. Zhang, H.-F. Song, M. Troyer, and A. A.Soluyanov, Comput. Phys. Commun. **224**, 405 (2018).

[40] K. Schwarz and P. Blaha, Comput. Mater. Sci. **28**, 259 (2003).

[41] J. Gao, Q. Wu, C. Persson, and Z. Wang, Comput. Phys. Commun. **261**, 107760 (2021).

[42] E. Bjerkelund, J. Fermor, and A. Kejekshus, Acta chem. Scand. **20**, 1836 (1966).

[43] S. Tang, C. Zhang, D. Wong, Z. Pedramrazi, H.-Z. Tsai, C. Jia, B. Moritz, M. Claassen, H. Ryu, S. Kahn, J. Jiang, H. Yan, M. Hashimoto, D. Lu, R. G. Moore, C.-C. Hwang, C. Hwang, Z. Hussain, Y. Chen, M. M. Ugeda, Z. Liu, X. Xie, T. P. Devereaux, M. F. Crommie, S.-K. Mo, and Z.-X. Shen, Nat. Phys. **13**, 683 (2017).

[44] P. Zhang, P. Richard, T. Qian, Y.-M. Xu, X. Dai, and H. Ding, Rev. Sci. Instrum. **82**, 043712 (2011).

[45] Y. Kim, H. Oh, C. Kim, D. Song, W. Jung, B. Kim, H. J. Choi, C. Kim, B. Lee, S. Khim, H. Kim, K. Kim, J. Hong, and Y. Kwon, Phys. Rev. B **83**, 064509 (2011).

[46] Z. Ringel, Y. E. Kraus, and A. Stern, Phys. Rev. B **86**, 045102 (2012).

[47] S. Kim, S. Yoshizawa, Y. Ishida, K. Eto, K. Segawa, Y. Ando, S. Shin, and F. Komori, Phys. Rev. Lett. **112**, 136802 (2014).